Journal of Materials Chemistry A

Accepted Manuscript

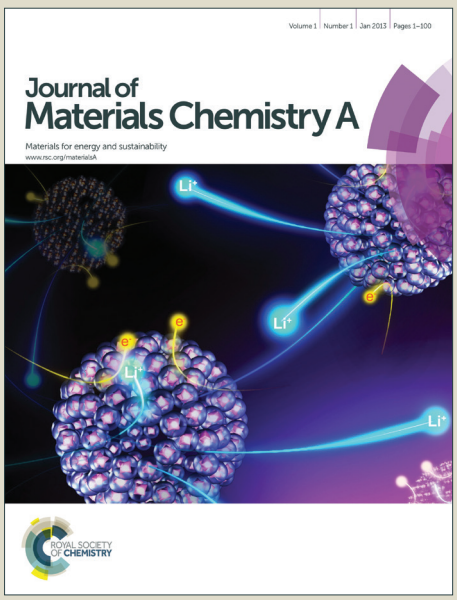

ROYAL SOCIETY OF CHEMISTRY

www.rsc.org/materialsA

Journal of Materials Chemistry A RSCPublishing

COMMUNICATION

α-Fe_2O_3 on patterned fluorine doped tin oxide for efficient photoelectrochemical water splitting

Cite this: DOI: 10.1039/x0xx00000x

Kwanghyun Kim, Ik-Hee Kim, Ki-Yong Yoon, Jeong-Yeop Lee and Ji-Hyun Jang*

Received 00th January 2012,
Accepted 00th January 2012

DOI: 10.1039/x0xx00000x

www.rsc.org/

Patterned FTO was fabricated via a facile method as an efficient current collector in a photoelectrochemical water splitting system. The photocurrent density of α-Fe_2O_3 on patterned FTO exhibited a 1.7 times increase relative to α-Fe_2O_3 on FTO due to the light scattering and rapid transfer of excited electrons.

In the last decade, the generation of hydrogen gas has been extensively studied as a promising method for renewable green energy sources. Among its most attractive features are that it does not create byproducts of pollutants during the energy generation reaction and it can be directly applied as a fuel for combustion. Hydrogen gas can be easily obtained from water molecules via the photocatalytic process of water splitting in photoelectrochemical (PEC) systems. In order to enable PEC water splitting, a semiconductor material that can efficiently absorb the energy of sunlight is necessary. A variety of semiconductor photoanode materials (TiO_2[1-3], ZnO[4, 5], WO_3[6, 7], etc.) have been studied in the context of criteria such as cost effectiveness, chemical stability, and proper bandgap energy and band edge position in the energy diagram. As the PEC water splitting field has rapidly developed, interest in the working capability under visible light, which occupies nearly half of the portion of sunlight, has gradually increased. Materials that have small bandgap energy falling into the visible region thus have become essential for efficient water splitting systems.

α-Fe_2O_3 (hematite) has attracted a great deal of attention due to the advantages of a low bandgap energy of 2.1 ~ 2.2 eV, which covers the visible light range, and low cost, stability, and abundance.[8, 9] Despite these advantages, some factors that cause high recombination rates, such as short carrier lifetime (~ 1 ps)[10], poor light absorption near the band edge[11], and very short hole diffusion length ranging in a few nanometers[12, 13] must still be overcome. These problems have restricted the charge separation and charge collection properties accordingly, resulting in significantly degraded performance. To date, many strategies have been explored to overcome the aforementioned limitations of hematite for PEC devices by enhancing the electronic and optical properties; i.e. nanostructuring the photoelectrodes (nanotubes, nanowires, flower shape and inverse opal etc.)[14-18] and doping with some heteroatoms (Sn, Co and Ti etc.)[16, 19-21] etc. Alternatively, interlayer structures with better crystallinity between the current collector and the hematite structures were suggested for facile transport of electrons to the electrode.[22] Building a p-n junction at the interface of NiO/hematite[23] or silicon/hematite[24] helps deliver the generated electrons toward the current collector before recombination occurs. Several enhanced conductive materials such as antimony-doped tin oxide (ATO), gold, graphene, carbon nanotubes (CNTs) etc.[25-28] have been researched for the same reason.

Fluorine doped tin oxide (FTO) is a widely used transparent conducting electrode in photo-electronic systems such as solar cells and PEC water splitting because of its remarkable

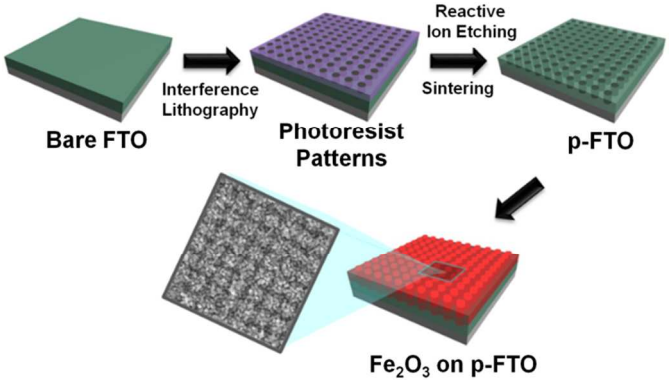

Scheme 1 Illustration for the fabrication of α-Fe_2O_3 on p-FTO.

advantages in cost and chemical stability. Recently, patterned-FTO (p-FTO) having light scattering effects has been suggested as an efficient conducting layer in DSSCs[23].

We hypothesized that a three dimensional p-FTO structure could serve as not only a light scattering layer, but also a direct electron transporting network with very facile processes in a PEC water splitting system. It was found that a worm-like hematite structure coated on a p-FTO exhibits a photocurrent density of 1.88 mA/cm^2, a 1.7 times increase in comparison with a corresponding structure on an unpatterned FTO substrate.

SU-8 coated FTO using SU-8 patterns as a mask. The residues of the photoresists were removed by sintering at high temperature. The worm-like hematite was deposited on p-FTO by a method reported elsewhere. The details of sample preparation are discussed in the experimental part of Supplementary Information.

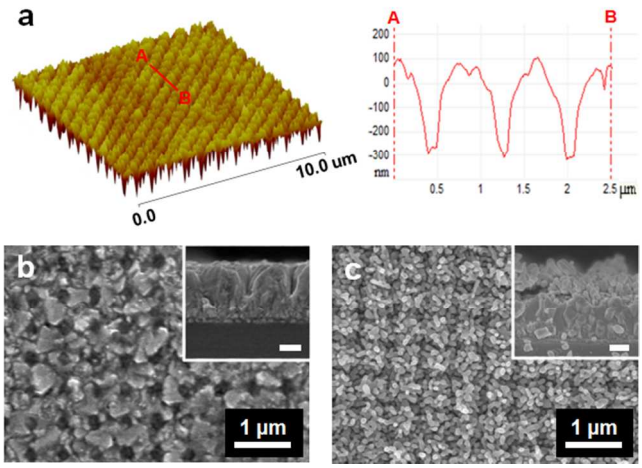

Fig. 1 Atomic force microscope (AFM) and scanning electron microscope (SEM) images of p-FTO and patterned α-Fe_2O_3 on p-FTO. a) The three-dimensional surface morphology and the depth profile of p-FTO, b) Top view and side view of p-FTO (inset image, scale bar is 250 nm), and c) Top view and side view of α-Fe_2O_3/p-FTO (inset image, scale bar is 250 nm).

The morphologies of p-FTO and patterned α-Fe_2O_3 on p-FTO are characterized by atomic force microscopy (AFM) and scanning electron microscopy (SEM) observations. The height and the pitch of the SU-8 patterns were about 400 nm and 560 nm, respectively, as shown in Fig. S1. The morphology of p-FTO after RIE and the annealing steps to remove the residues of the SU-8 patterns is shown in Fig. 1a and 1b. The detailed conditions

of the RIE process are provided in the experimental part of Supplementary Information. Uniform height and a clear hole shape were difficult to achieve due to the rough surface of bare FTO. Fig. 1c shows the worm-like hematite layer with a similar overall morphology to that of p-FTO. The worm-like α-Fe_2O_3 is one of the well-known hematite structures that has shown excellent performance in PEC systems.[8] The patterned worm-like hematite materials were densely grown on p-FTO, as shown in Fig. 1c, proving strong potential for a large surface area and light scattering caused by the interactions between the periodically aligned patterned-structure and the exposed light.

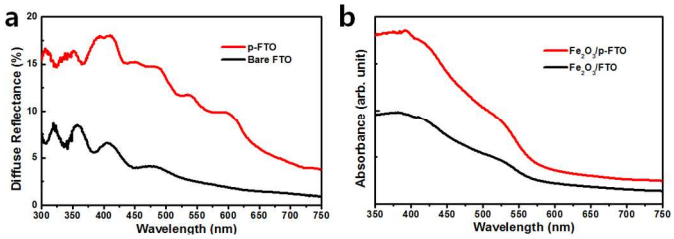

Fig. 2 Optical properties of α-Fe_2O_3/bare FTO and α-Fe_2O_3/p-FTO: a) Diffuse reflectance and b) absorption spectra.

Fig. 2 shows the optical properties of p-FTO through an analysis of the UV-visible spectroscopy results. The diffuse reflectance in Fig. 2a compares the degree of light scattering of bare FTO and p-FTO. The 3D p-FTO improves light scattering effects in the visible range due to the nanostructures that interact well with the exposing light. It has been reported that the direction of incident light changes in a variety of ways when meeting different media. The effect can be larger with certain materials having a rough surface or periodic structure on a hundreds of nanometer scale and a large refractive index. The large intensity of light scattering accounts for the longer pathways of light in the structure, as shown in the schematic image (Fig. S4). The light absorbance is very important because it is strongly related with how much of the light is utilized for the generation of photocurrent in the PEC cells. Ultimately, the substantially enhanced light scattering effect of p-FTO with a three-dimensional structure improves the light

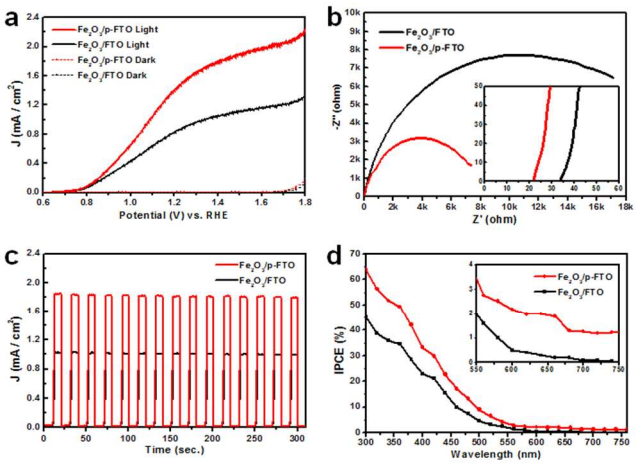

Fig. 3 The photoelectrochemical properties of α-Fe_2O_3 on bare FTO and p-FTO (a) Linear sweep voltammetry curves (LSV, photocurrent - potential curves) of α-Fe_2O_3/FTO and p-FTO under UV-visible light and dark conditions. (b) Nyquist plots of α-Fe_2O_3/FTO and α-Fe_2O_3/p-FTO to investigate the electrochemical impedance spectroscopy (EIS) responses. (c) Photocurrent–time (J-t) curves of α-Fe_2O_3/FTO and α-Fe_2O_3/p-FTO at a bias of 1.5 V vs. RHE under UV-visible light illumination. (d) Measurement of the incident photon-to-electron conversion efficiency.

absorption of the catalyst, and thus enhances the photocurrent under the UV-visible region. The greatly increased absorption of α-Fe_2O_3 coated on p-FTO compared with bare FTO over all wavelength regions is shown in Fig. 2b. The Tauc plots in Fig. S6 also imply smaller bandgap due to enhanced absorption in α-Fe_2O_3/p-FTO.

The photocurrent densities of α-Fe_2O_3 on bare FTO and p-FTO were measured at a potential range from 0.4 V to 2 V vs. RHE under AM 1.5 G simulated sunlight illumination, as shown in Fig. 3a. α-Fe_2O_3/FTO and α-Fe_2O_3/p-FTO respectively had a photocurrent density of 1.1 mA/cm^2 and 1.88 mA/cm^2 at 1.5 V vs. RHE. Compared to the photocurrent density of α-Fe_2O_3, which is similar to the values reported in other α-Fe_2O_3 studies,[15] the value on p-FTO is 1.7 times higher under UV-visible light illumination. This improvement can be attributed to enhanced light absorption and rapid transfer of photogenerated electrons. p-FTO enables i) the light to have longer paths via efficient scattering, and thus enhanced absorption, and ii) photogenerated electrons to reach the current collector rapidly by providing a shorter migration length between α-Fe_2O_3 and the three-dimensional current collector substrate, as described in the schematic diagram (Fig. S4).

In order to explore the improved electron transfer behavior of α-Fe_2O_3/p-FTO, the EIS responses of α-Fe_2O_3/FTO and α-Fe_2O_3/p-FTO were measured in 1 M NaOH electrolyte at a frequency range from 100 kHz to 0.1 Hz under illumination of AM 1.5 G, as shown in Fig. 3b. The intercepts with the real axis at the high–frequency region represent the R_s (equivalent series resistance) values, corresponding to the contact resistance between the α-Fe_2O_3 electrode material and the current collector substrate. The lower R_s value of α-Fe_2O_3/p-FTO (21.9 Ω) than that of α-Fe_2O_3/FTO (33.7 Ω) implies facile transport of electrons achieved by short migration paths through the α-Fe_2O_3 active material directly contacting the 3D p-FTO current collector. The diameter of the semicircle at the middle frequency region is related with R_{ct}, which corresponds to the interfacial charge transfer resistance between the α-Fe_2O_3 layer and the electrolyte. α-Fe_2O_3/p-FTO had a lower R_{ct} value, indicating improved transport behavior of holes due to a decrease of bulk recombination achieved by the rapid transfer of electrons to the 3D-current collector.

The current density-time curves of α-Fe_2O_3 on bare FTO and p-FTO were obtained by a chopped illumination of AM 1.5 G at an interval of 10 s on/off for UV-visible light at 1.5 V vs. RHE (Fig. 3c). The abrupt occurrence and decay of the photocurrent density with sharp rectangular shapes during the on/off illumination sequence implies fast conduction of photo-generated electrons from α-Fe_2O_3 to p-FTO. Photocurrent in the J-t curves remained constant and closely matched that of the J-V curves in Fig. 3a, indicating that the α-Fe_2O_3 materials are very stable over many cycles.

The incident photon-to-electron conversion efficiency (IPCE), with a rapid increase at about 580 nm corresponding to roughly 2.14 and 2.17 eV band gap energy of α-Fe_2O_3/FTO and α-Fe_2O_3/p-FTO, is shown in Fig. 3d. The IPCE curve of α-Fe_2O_3/p-FTO slightly increased at about 675 nm wavelength. The IPCE value of 65 % at 300 nm α-Fe_2O_3/p-FTO showed overall improved performance compared with α-Fe_2O_3/bare FTO. This is consistent with the result of Tauc plots in Fig. S6.

Conclusions

Despite the very attractive properties of hematite as a photoanode in water splitting systems, many limitations remain. We overcome these issues by simply coupling a three-dimensionally and periodically patterned current collector, p-FTO, with worm-like α-Fe_2O_3. p-FTO was fabricated by a facile RIE method of SU-8 square patterns generated via interference lithography on a commercial FTO substrate. p-FTO provides enhanced light scattering effects and rapid and direct transfer pathways to the current collectors, leading to enhancement of the photocurrent density achieved by reducing recombination of photogenerated electrons and holes. Hematite on p-FTO showed 1.7 times improved photocurrent density relative to the corresponding structure on bare FTO. This is meaningful since key problems of hematite photoanodes for photoelectrochemical water splitting were overcome efficiently by simple patterning of the current collectors.

Acknowledge

This work is supported by NRF with the contract no. NRF-2010-0019408 and 2014-M2B2A4030415 (National nuclear R&D program, MSIP) and by Ministry of Trade, Industry & Energy of Korea (10040038).

Notes and references

School of Energy and Chemical Engineering, Low Dimensional Carbon Materials Center, 689-798, UNIST, Korea. Fax: +82-52-217-3008; Tel: +82-52-217-2922; E-mail: clau@unist.ac.kr

† Electronic Supplementary Information (ESI) available: [details of any supplementary information available should be included here]. See DOI: 10.1039/b000000x/

1. R. Raja, P. Sudhagar, A. Devadoss, C. Terashima, L. K. Shrestha, K. Nakata, R. Jayavel, K. Ariga and A. Fujishima, *Chemical Communications*, 2015, **51**, 522-525.
2. K. Kim, P. Thiyagarajan, H.-J. Ahn, S.-I. Kim and J.-H. Jang, *Nanoscale*, 2013, **5**, 6254-6260.
3. K. Kim, M.-J. Kim, S.-I. Kim and J.-H. Jang, *Sci. Rep.*, 2013, **3**.
4. T. Wang, R. Lv, P. Zhang, C. Li and J. Gong, *Nanoscale*, 2015, **7**, 77-81.
5. A. Kargar, Y. Jing, S. J. Kim, C. T. Riley, X. Pan and D. Wang, *ACS Nano*, 2013, **7**, 11112-11120.
6. H. Zheng, J. Z. Ou, M. S. Strano, R. B. Kaner, A. Mitchell and K. Kalantar-zadeh, *Advanced Functional Materials*, 2011, **21**, 2175-2196.
7. D.-D. Qin, C.-L. Tao, S. A. Friesen, T.-H. Wang, O. K. Varghese, N.-Z. Bao, Z.-Y. Yang, T. E. Mallouk and C. A. Grimes, *Chemical Communications*, 2012, **48**, 729-731.
8. J. Y. Kim, G. Magesh, D. H. Youn, J.-W. Jang, J. Kubota, K. Domen and J. S. Lee, *Sci. Rep.*, 2013, **3**.

9. M. Marelli, A. Naldoni, A. Minguzzi, M. Allieta, T. Virgili, G. Scavia, S. Recchia, R. Psaro and V. Dal Santo, *ACS Applied Materials & Interfaces*, 2014, **6**, 11997-12004.
10. A. G. Joly, J. R. Williams, S. A. Chambers, G. Xiong, W. P. Hess and D. M. Laman, *Journal of Applied Physics*, 2006, **99**, -.
11. K. Sivula, R. Zboril, F. Le Formal, R. Robert, A. Weidenkaff, J. Tucek, J. Frydrych and M. Grätzel, *Journal of the American Chemical Society*, 2010, **132**, 7436-7444.
12. H.-J. Ahn, M.-J. Kwak, J.-S. Lee, K.-Y. Yoon and J.-H. Jang, *Journal of Materials Chemistry A*, 2014, **2**, 19999-20003.
13. M. Barroso, S. R. Pendlebury, A. J. Cowan and J. R. Durrant, *Chemical Science*, 2013, **4**, 2724-2734.
14. H. Jun, B. Im, J. Y. Kim, Y.-O. Im, J.-W. Jang, E. S. Kim, J. Y. Kim, H. J. Kang, S. J. Hong and J. S. Lee, *Energy & Environmental Science*, 2012, **5**, 6375-6382.
15. D. A. Wheeler, G. Wang, Y. Ling, Y. Li and J. Z. Zhang, *Energy & Environmental Science*, 2012, **5**, 6682-6702.
16. Y. Ling, G. Wang, D. A. Wheeler, J. Z. Zhang and Y. Li, *Nano Letters*, 2011, **11**, 2119-2125.
17. X. Shi, K. Zhang, K. Shin, J. H. Moon, T.-W. Lee and J. H. Park, *Physical Chemistry Chemical Physics*, 2013, **15**, 11717-11722.
18. Y. Qiu, S.-F. Leung, Q. Zhang, B. Hua, Q. Lin, Z. Wei, K.-H. Tsui, Y. Zhang, S. Yang and Z. Fan, *Nano Letters*, 2014, **14**, 2123-2129.
19. R. H. Goncalves and E. R. Leite, *Energy & Environmental Science*, 2014, **7**, 2250-2254.
20. Y. Hou, F. Zuo, A. Dagg and P. Feng, *Angewandte Chemie International Edition*, 2013, **52**, 1248-1252.
21. J. Baltrusaitis, Y.-S. Hu, E. W. McFarland and A. Hellman, *ChemSusChem*, 2014, **7**, 162-171.
22. O. Zandi, J. A. Beardslee and T. Hamann, *The Journal of Physical Chemistry C*, 2014, **118**, 16494-16503.
23. F. Wang, N. K. Subbaiyan, Q. Wang, C. Rochford, G. Xu, R. Lu, A. Elliot, F. D'Souza, R. Hui and J. Wu, *ACS Applied Materials & Interfaces*, 2012, **4**, 1565-1572.
24. M. T. Mayer, Y. Lin, G. Yuan and D. Wang, *Accounts of Chemical Research*, 2013, **46**, 1558-1566.
25. K.-Y. Yoon, J.-S. Lee, K. Kim, C. H. Bak, S.-I. Kim, J.-B. Kim and J.-H. Jang, *ACS Applied Materials & Interfaces*, 2014.
26. J. Young Kim, J.-W. Jang, D. Hyun Youn, J. Yul Kim, E. Sun Kim and J. Sung Lee, *RSC Advances*, 2012, **2**, 9415-9422.
27. Y. Sun, W. D. Chemelewski, S. P. Berglund, C. Li, H. He, G. Shi and C. B. Mullins, *ACS Applied Materials & Interfaces*, 2014, **6**, 5494-5499.
28. C. H. Bak, K. Kim, K. Jung, J.-B. Kim and J.-H. Jang, *Journal of Materials Chemistry A*, 2014, **2**, 17249-17252.

Table of Contents

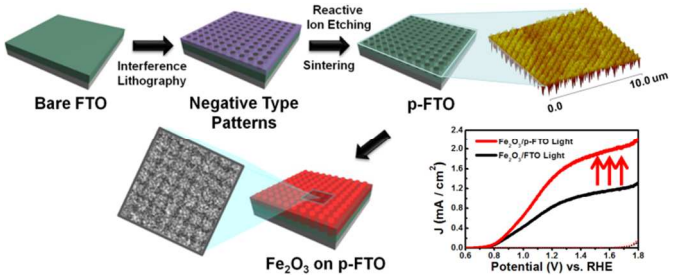

By simply pattering conductive FTO in a 3D-shape, we achieved 1.7 times greater photocurrent density in water splitting reactions.

Fe_2O_3 on patterned fluorine doped tin oxide for efficient photoelectrochemical water splitting

Kwanghyun Kim, Ik-Hee Kim, Ki-Yong Yoon, Jeong-Yeop Lee and Ji-Hyun Jang*

Preparation of patterned FTO (p-FTO)

The FTO substrate was washed by sequential ultrasonication in acetone, isopropanol, deionized water, and ethanol for 10min. each followed by nitrogen blowing. A SU-8 solution (SU-8:CP = 1:2.25) was spin-coated on the cleaned FTO at 3000rpm for 30s followed by prebaking on a hotplate at 100^{o}C for 30min. The photoresist-coated FTO was double-exposed under a 365nm laser source to make square patterns via interference lithography. To determine the pitch distance and the hole diameter of the patterns, the angle of Lloyd′s mirror and the time of exposure were varied. The exposed samples were post-baked on the hotplate at 70^{o}C for 10min. The unexposed regions were then removed in a propylene glycol monomethyletheracetate solution for a minute and washed in isopropyl alcohol for 30s, resulting in SU-8 square patterns.

Reactive ion etching (RIE) was performed to vertically etch FTO. The plasma was generated at a pressure of 40mTorr with a RF power of 300W. The gas pressure ratio of CF_4, CHF_3, Ar, and O_2 was around 2:9:1:1. p-FTO was created after removal of the residue of SU-8 by annealing at 500^{o}C for an hour.

Preparation of the α-Fe_2O_3 on p-FTO

The fabrication of the worm-like α-Fe_2O_3 layer followed the procedure previously reported by this group.[1] 30ml of a 150mM $FeCl_3 \cdot 6H_2O$ aqueous solution was transferred into a Teflon-lined autoclave, and the substrates were reclined on the inside of the autoclave facing the p-FTO side to the wall. After 6hrs of reaction at 100^{o}C, a uniform layer of FeOOH was

formed on the p-FTO substrate. The substrates were thoroughly rinsed with D.I. water and ethanol. The samples were then annealed at 550^{o}C in air for one hour to convert FeOOH to a hematite film. To enhance the crystallinity of hematite, the samples were further annealed at 800^{o}C in air for 20min.

Photoelectrochemical measurement

The PEC performance of α-Fe_2O_3 on p-FTO was explored in a three-cell electrode system under front-side illumination of AM 1.5G and 100mW/cm^2 using 300W power from a Xe lamp. An Ag/AgCl (KCl sat.) electrode and a Pt mesh were used a reference and counter electrode, respectively. A solution of 1M NaOH (pH 13.6) was used as an electrolyte. The exposed area of the working electrode was set to be 0.25cm^2 by making a window with scotch tape. Photocurrent stability tests were carried out by measuring the photocurrent produced under chopped light irradiation (light/dark cycles of 10s.) at a bias of 1.5V vs. RHE. EIS was carried out at a frequency range from 100kHz to 0.1Hz.

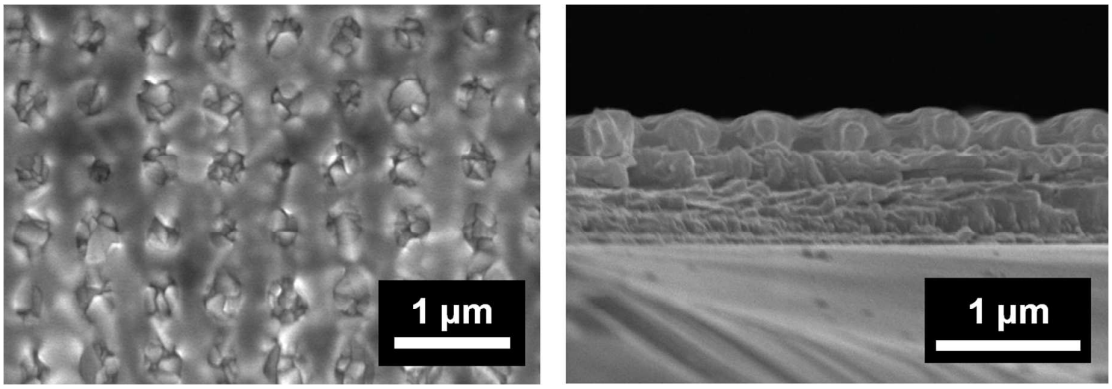

Figure S1. SEM images of SU-8 patterns on FTO; the top view and cross-section view.

The SU-8 layer on the FTO substrate has square patterns with a height of about 300nm and a pitch distance of about 550nm. Its appearance is very important to determine the etched shape of FTO because the RIE passes off vertically.

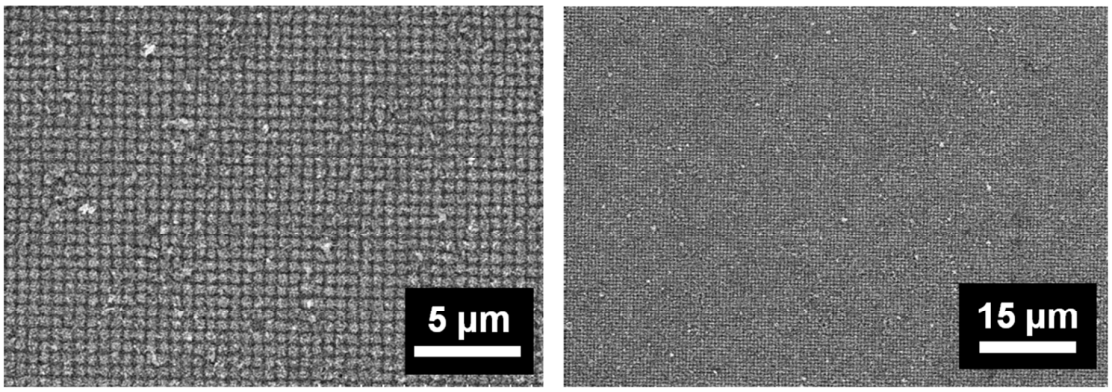

Figure S2. Wide view SEM images of Fe_2O_3/p-FTO.

After coating the worm-like hematite layer on p-FTO, a patterned worm-like hematite layer with a periodically well-aligned shape over a very large area was created as shown in **Figure S2**.

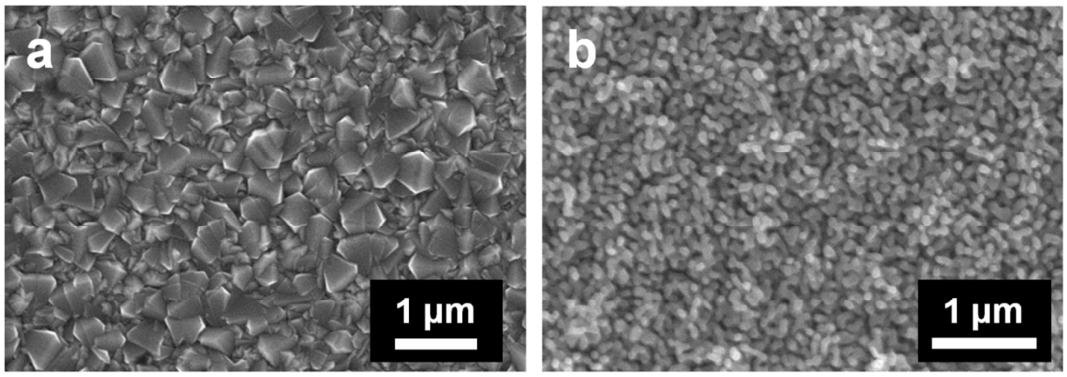

Figure S3. SEM images of a) bare FTO, b) the worm-like shape hematite layer on bare FTO.

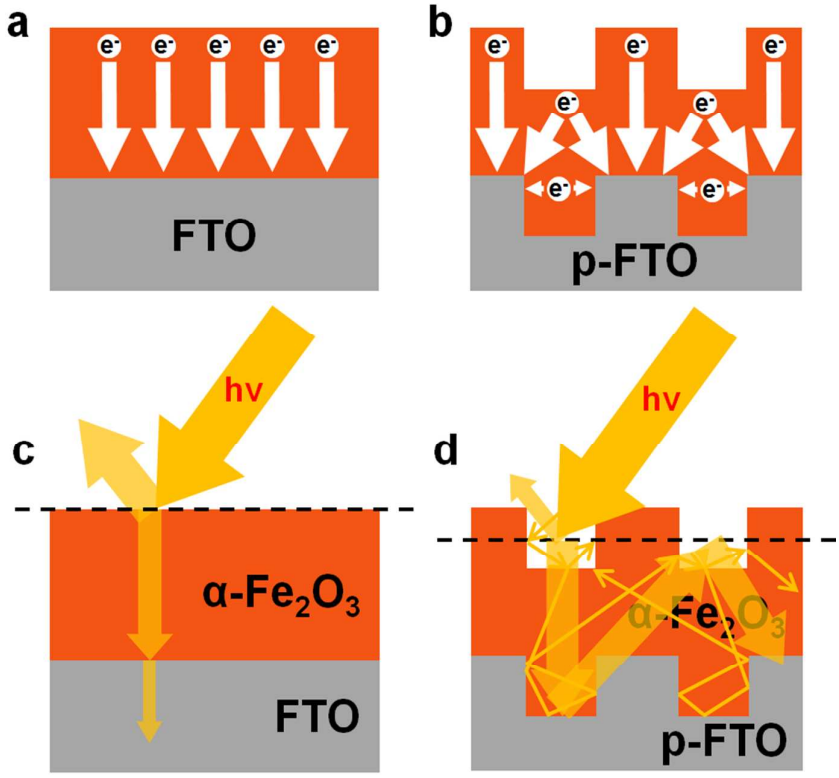

Figure S4. Schematic diagrams that show a), b) the shorter migration pathway of the photogenerated electrons and c), d) the greater scattering of incident sunlight in α-Fe_2O_3/p-FTO than α-Fe_2O_3/bare FTO.

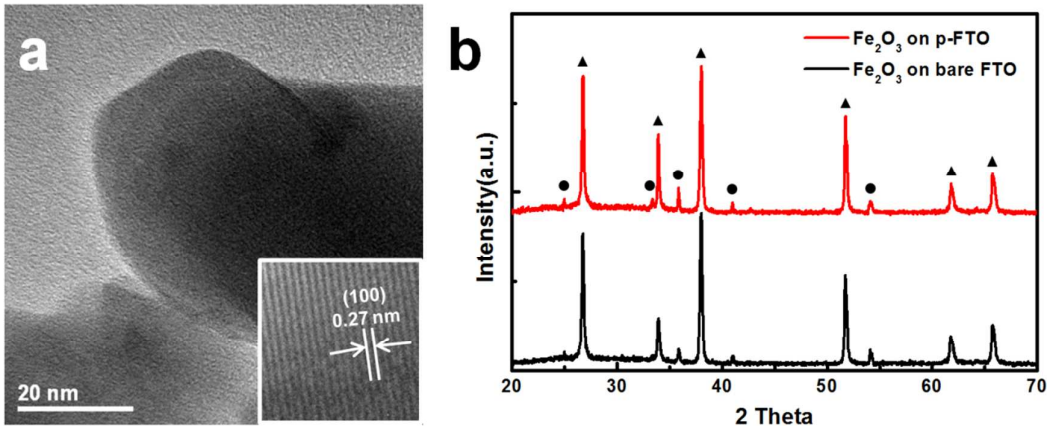

Figure S5. The crystalline hematite material confirmed using TEM and XRD. a) TEM image of the worm-like hematite. The d-spacing in the inset is shown as about 0.27nm

corresponding to the (100) plane of hematite. b) XRD data of Fe_2O_3 on p-FTO and bare FTO. (▲ indicates the FTO and ● is marked at the peaks of hematite.)

The crystallinity of α-Fe_2O_3/FTO and α-Fe_2O_3/p-FTO was investigated by TEM and XRD. d-spacing of about 0.27nm in the inset image in **Figure S5a** confirms the presence of hematite and **Figure S5b** presents proper peaks corresponding to the hematite of α-Fe_2O_3.

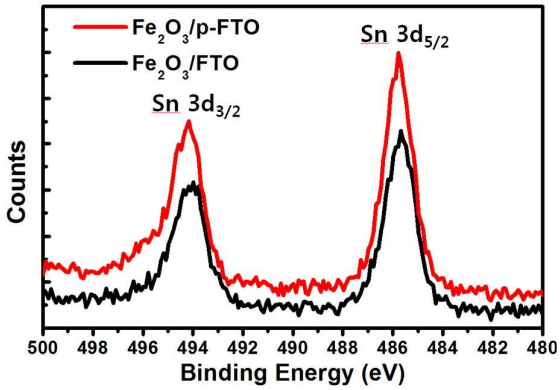

Figure S6. XPS spectra of Sn 3d core levels of the Fe_2O_3/p-FTO and Fe_2O_3/FTO.

XPS depth profiles of α-Fe_2O_3/FTO and α-Fe_2O_3/p-FTO were obtained in order to check the possibility of Sn doping. Sn doping onto FTO occurred during high temperature annealing step (800°C, 20min.), which was done to enhance the crystallinity of hematite.[2] α-Fe_2O_3/p-FTO with a larger contact area between α-Fe_2O_3 and 3D-shaped FTO was slightly more doped with Sn than FTO, which also might permit the positive effect of patterning FTO on PEC performance.

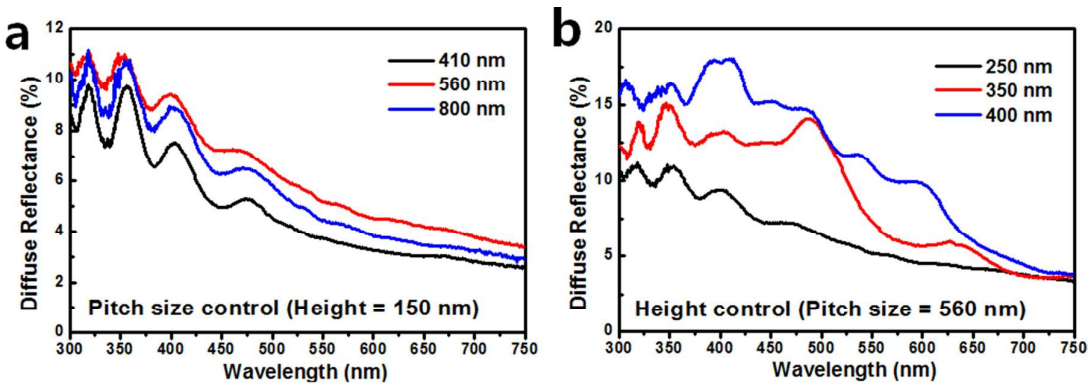

Figure S7. Diffuse reflectance data of a) pitch size and b) height controlled p-FTO samples with fixed the other condition.

We performed diffuse reflectance measurements on p-FTO by varying the pitch size (**Figure S7a**) and height (**Figure S7b**). As can be seen in the diffuse reflectance data, the absorbance of Fe_2O_3/p-FTO with a 560nm of pitch size and a 400nm of height is the greatest, so we optimized the p-FTO with those parameters.

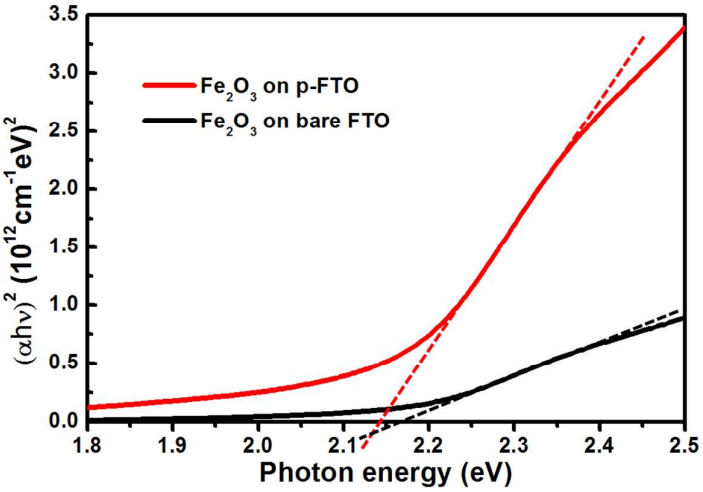

Figure S8. Tauc plots calculated using absorbance data of UV-visible spectroscopy.

The band gap energy of α-Fe_2O_3/FTO and α-Fe_2O_3/p-FTO was obtained by a Tauc plot, which was calculated through the absorbance data in **Figure 2b**.[3] **Figure S8** shows that band gap energy of about 2.14eV and 2.17eV was obtained for α-Fe_2O_3/FTO and α-Fe_2O_3/p-FTO, respectively. This value is consistent with the well-known band gap energy of hematite.

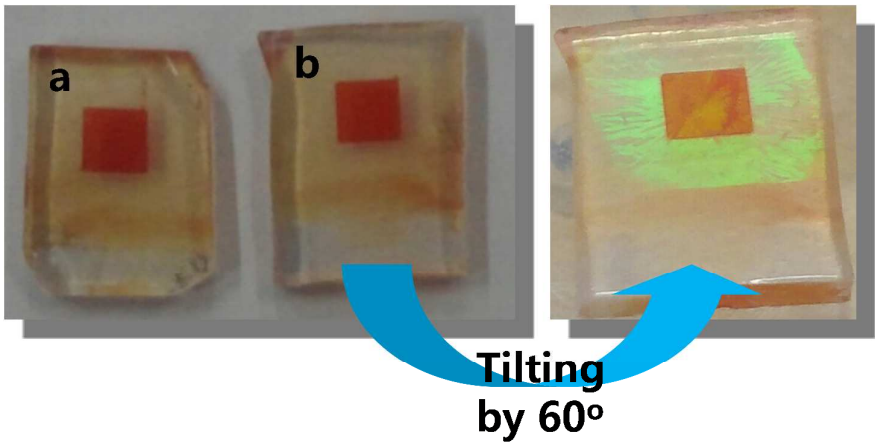

Figure S9. Digital camera image of α-Fe_2O_3/FTO(a) and α-Fe_2O_3/p-FTO(b).

The rainbow color in the background of α-Fe_2O_3/p-FTO with a tilted angle of incident light indicates the presence of the periodic patterns on the surface of FTO.

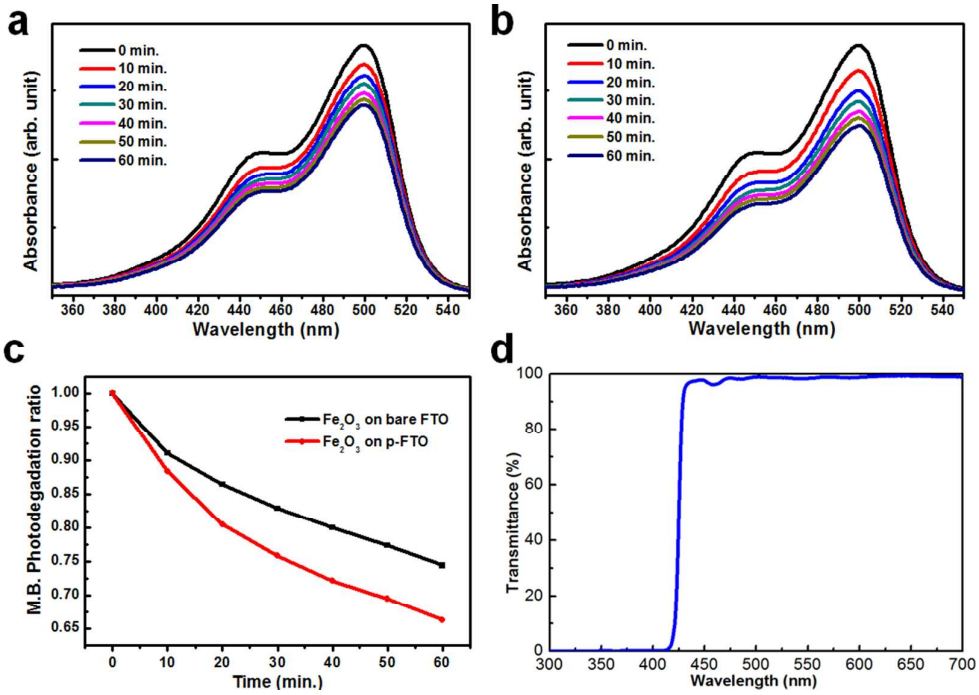

Figure S10. Methylene blue photodegradation ratio for the case of α-Fe_2O_3/FTO and α-Fe_2O_3/p-FTO under visible light illumination (λ > 420nm) using a UV cutoff filter. Absorbance data of the methylene blue solution during photodegradation of a) α-Fe_2O_3/FTO and b) α-Fe_2O_3/p-FTO. c) Photodegradation ratio of MB for 60min. d) Transmittance data of used UV cutoff filter.

Figure S10 shows the photocatalytic effect of α-Fe_2O_3/FTO and α-Fe_2O_3/p-FTO confirmed via photodegradation of methylene blue (2.7×10^{-5}M). The absorbance peak of methylene blue appears in the region from 350nm to 550nm wavelength. 10ml solutions with α-Fe_2O_3/FTO and α-Fe_2O_3/p-FTO in 20ml vial were shone under visible light via a UV cutoff filter. **Figure S10c** shows the enhanced visible light photocatalytic property of α-Fe_2O_3/p-FTO, rather than α-Fe_2O_3 /FTO. As shown in **Figure S10d**, the wavelength of applied visible light was longer than 420nm. The absorbance curves of the two solutions were checked every 10min.

	Sheet resistivity [Ohm / square]	Thickness [nm]	Resistivity [Ohm · cm]
α-Fe_2O_3 on bare FTO	12.08	1427	1.72×10^{-3}
α-Fe_2O_3 on p-FTO	10.87	1265	1.38×10^{-3}

Figure S11. The electrical conductivity of α-Fe_2O_3/FTO and α-Fe_2O_3/p-FTO confirmed via 4-probe measurement.

References

1. H.-J. Ahn, M.-J. Kwak, J.-S. Lee, K.-Y. Yoon and J.-H. Jang, Journal of Materials Chemistry A, 2014, 2, 19999-20003.
2. J. Y. Kim, G. Magesh, D. H. Youn, J.-W. Jang, J. Kubota, K. Domen and J. S. Lee, Sci. Rep., 2013, 3.
3. J. Tauc, R. Grigorovici and A. Vancu, physica status solidi (b), 1966, 15, 627-637.